RSC Advances

ROYAL SOCIETY OF CHEMISTRY

www.rsc.org/advances

Cite this: DOI: 10.1039/c0xx00000x

www.rsc.org/xxxxxx

ARTICLE TYPE

$Fe_2(MoO_4)_3$ nanoparticles-anchored MoO_3 nanowires: strong coupling via the reverse diffusion of heteroatoms and largely enhanced lithium storage properties†

Yeping Song [ab], Hai Wang [ab*], Zihua Li [a], Naiqing Ye [a], Linjiang Wang [ab] and Yong Liu [c]

Received (in XXX, XXX) Xth XXXXXXXXX 20XX, Accepted Xth XXXXXXXXX 20XX

DOI: 10.1039/b000000x

A novel hierarchical heterostructural $Fe_2(MoO_4)_3$@MoO_3 (FM) nanowire is developed by mild hydrothermal treatment of precursor MoO_3 nanobelts only with the assistance of $FeCl_3.6H_2O$ combined with the heat treatment. Subsequently, a model of reverse heteroatoms diffusion is proposed to describe the formation of FM nanowires. Further, it is found that the heteroatoms diffusion and facet-selective growth of $Fe_2(MoO_4)_3$ on MoO_3 nanobelts brought about the change of MoO_3 morphology from nanobelts to nanowires, and $Fe_2(MoO_4)_3$ nanoparticles are firmly anchored onto MoO_3 nanowires. When tested as LIBs anodes, compared to pristine MoO_3 nanobelts, high reversible lithium storage capacities of anodes are obtained from novel FM nanowires. The electrode of FM nanowires obtained at 500 ℃ (FM-500) exhibits superior reversible capacity of 585 mAh g^{-1} retained at a current density of 100 mA g^{-1} after 100 cycles, and 518 mAh g^{-1} retained after 100 cycles at 200 mA g^{-1}. The distinct electrochemical activity of $Fe_2(MoO_4)_3$ nanoparticles probably activates the irreversible capacity of the MoO_3 nanobelts. Moreover, the amorphous layer and structure stability of heterojunction electrodes are also beneficial for charge storage, electron transfer and lithium ion diffusion during the charge-discharge process.

Introduction

The design and rational synthesis of electrode materials with high energy density, high rate capability, and good cyclability for lithium-ion batteries (LIBs) has been one of the hot topics. Compared with commercial graphite anodes with a specific capacity of 372 mAh g^{-1}, MoO_3 has long been considered as an attractive anode material for LIBs, due to its relatively high theoretical capacity of 1111 mAh g^{-1} [1]. However, its practical applications are still hindered by its relatively low specific capacities and rate properties that are caused by poor intrinsic ionic and electronic conductivity [1-3]. Designing MoO_3 nanobelts has been demonstrated to be an effective solution to overcome the aforementioned obstacles. Recent studies in these areas have revealed that fabricating conducting layer on the surface of MoO_3 nanobelts, employing carbon-coating, graphene and using lithiation technologies et al are several ideal strategies to enhance electrochemical performance of 1D MoO_3 nanobelts [1, 3-7]. But still, the performance of MoO_3 nanobelts-based anodes are not very satisfactory, especially the decay of capacity with long-term cycling.

NASICON-structured $Fe_2(MoO_4)_3$ has been identified as a potential candidate for sodium or lithium storage due to its cheap, non-toxic of iron and its open three dimensions framework [8, 9]. However, the lack of direct Fe-Fe or Fe-O-Fe interaction results in its poor electronic conductivity, low rate capability and bad cyclability despite good lithium ion conduction in the Nasicon-based frameworks.

Recently, numerous studies have been taken to fabricate heterogeneous metal oxides as promising anode materials for LIBs due to their higher energy density and longer cycle life [1, 4-6, 10, 11]. From the technological viewpoint, the composites may offer novel applications since they could take advantage of the synergistic effects between different constituent phases. To date, tremendous efforts has been devoted to choosing suitable LIBs materials and their assemblies in appropriate hierarchical heterostructures with smart composition and nanosized building blocks to achieve better performance, such as, α-Fe_2O_3@SnO_2 core-shell nanorattles [12], SnO_2@MoO_3 core-shell nanobelts [5], SnO_2@WO_3 core-shell nanorods [13,14], SnO_2@$ZnWO_4$ core-shell nanorods [15], $NiFe_2O_4$@Fe_2O_3 nanotubes [16], and so on. All these previous reports on hierarchical heterostructures composites mainly focused on the building blocks themselves. However, the building of the interface between the two different phases is considerably ignored. Generally, the interface between the individual component at a nanoscale provides a key platform to guarantee a fast continuous ion and electron transfer, thus leading to superior lithium-storage performance. For example, Fe_2O_3@SnO_2 [17, 18], Fe_2O_3@MnO_2 [19], SnO_2@WO_3 [13], SnO_2@MoO_3 [5], Co_3O_4@Fe_2O_3 [20], et al hierarchical heterostructures composites with good contact between two materials showed high electrochemical performance for Li-ion batteries. It seems that epitaxial growth and heterogeneous nucleation may be a more attractive way for building an idea interface. Nevertheless, the match of crystal lattice is a basic requirement, which greatly limits the choice of materials. Therefore, building new interface model is highly desired and important for the applications of LIBs.

Here, we present an alternative route by constructing novel hybrid metal oxide core/shell nanowires for LIBs. This unique designed electrode has the following advantages. First, both the core and shell metal oxides materials are good LIBs electrode materials (e.g., MoO_3, $Fe_2(MoO_4)_3$). Second, compared with the previous fabricated heterogeneous metal oxides, the way of $Fe_2(MoO_4)_3$ nanoparticles firmly anchored onto the MoO_3 nanobelts via the reverse diffusion of heteroatoms is mechanically stable and favourable especially for the cycling performance during charge-discharge process at high current densities. Third, the connection between $(101)_{MoO3}$ and $(202)_{Fe2(MoO4)3}$ leads to a continuous interface, which is beneficial for the transfer of the charge carriers. For this electrode design, not only all the desired functions of each constituent can be utilized effectively, but also a strong synergistic effect can be realized. Further, the interface relationship between MoO_3 and $Fe_2(MoO_4)_3$ would be clarified. To prove this concept, we choose MoO_3 and $Fe_2(MoO_4)_3$ as the model shell and core materials, respectively. It is found that, the FM-500 hybrid nanowires exhibit a high specific capacity of more than 3-fold compared with pristine MoO_3 nanobelts, according to the good cycle performance of 585 mA h g^{-1} after 100 cycles and remarkable rate capability at a current density of 100 mA g^{-1}.

Experimental

Materials synthesis

All chemical reagents were commercial products used without further purification. Firstly, MoO_3 nanobelts were prepared via a facile hydrothermal approach, according to reported studies [21]. Typically, 1 g of ammonium molybdate was dissolved in 30 mL of deionized water under continuous stirring. After 30 min, 6 mL of HNO_3 was added to the beaker dropwisely and stirred for another 30 min. The homogeneous suspension was formed. Then the resulting suspension was transferred to a Teflon-lined autoclave with a capacity of 50 mL and then kept inside an electric oven at 180 °C for 24 h. The as-prepared MoO_3 nanobelts powder was collected by filtration and thoroughly washed with deionized water and ethanol for several times and finally dried in air.

The fabrication of the $Fe_2(MoO_4)_3$@MoO_3 nanowires was carried out by a soaking hydrothermal process combined with post-heating treatment. Scheme 1 illustrates the formation process of the $Fe_2(MoO_4)_3$@MoO_3 nanowires. In a typical synthesis, first, 0.6 g of $FeCl_3$•$6H_2O$ was added into 60 mL deionized water, and 0.2 g of as-prepared MoO_3 powder was subsequently added into the above solution with magnetic stirring for 1 h. Then, the suspension was transferred to a 100 mL autoclave at 90 ℃ for 6 h. The hydrothermal sample was centrifuged and washed using deionized water and ethanol for several times, and dried under vacuum. Finally, the as-obtained sample is calcined at 500 ℃ (denoted as $Fe_2(MoO_4)_3$@MoO_3 -500, FM-500) and 600 ℃ for 2 h (denoted as $Fe_2(MoO_4)_3$@MoO_3-600, FM-600), respectively. To investigate the formation process of final $Fe_2(MoO_4)_3$@MoO_3 nanowires, the samples after the hydrothermal treatment of MoO_3 nanobelts-soaked with $FeCl_3$•$6H_2O$ solution are annealed at 200 ℃ (denoted as MoO_3-200) and 400 ℃ (denoted as MoO_3-400) for 2 h, respectively.

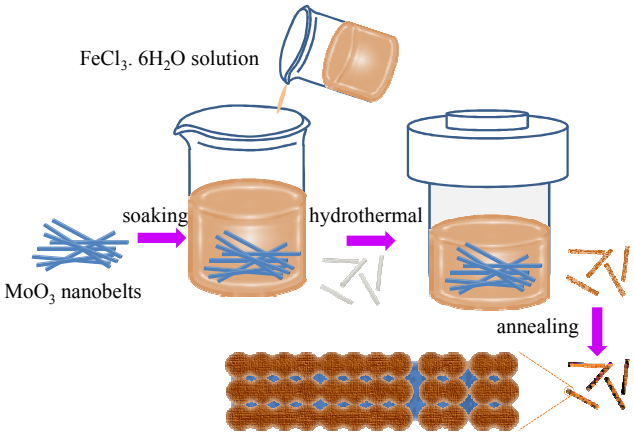

Scheme 1 Schematic representation for the preparation of the $Fe_2(MoO_4)_3$@MoO_3 nanowires by soaking and annealing process.

Characterization

The crystal structure was performed by X-ray diffraction (XRD) analysis with a PANanalytic X'Pert spectrometer using Cu K_α radiation with wavelength of 0.15405 nm. The surface morphologies of the samples were studied using a JEOL JSM6300 (Tokyo, Japan) field emission scanning electron microscope (FESEM). The transmission electron microscopy (TEM) and high-resolution transmission electron microscopy (HRTEM) images were obtained with a JEM-2010F electron microscope (JEOL, Japan) operating at 200 kV. The specific surface area and the pore size distribution (BJH method, desorption branch) were determined by nitrogen adsorption–desorption isotherms (Micromeritics, ASAP 2010). TG and DSC analysis of the samples were conducted on TGA 2050 thermo-gravimeter with a heating rate of 10 °C min^{-1} in air.

Electrochemical measurements

The electrochemical performance of as-prepared samples was tested by employing CR2025-type coin cells at room temperature. The working electrode included active material, acetylene black and PVDF in a 50 : 30 : 20 weight ratio. For electrochemical characterization, electrodes were prepared on aluminium foil (0.2 mm thick) as a current collector. A circular Al foil of area 1 cm^2 was cleaned with detergent. Coating were repeated to get the required loading level (2-3 mg) of the active material. A Celgard 3400 membrane was used as a separator and 1.0M $LiPF_6$ in a mixture of ethylene carbonate and diethyl carbonate (1 : 1 volume, Novolyte Technologies, USA) was used as the electrolyte. The cell was made in an argon-filled glovebox. The charge-discharge cycling performance and cyclic voltammetry (CV) (0.01-3.0 V, 0.2 mV s^{-1}) were carried out at room temperature by using a battery testing system (NEWARE) at different current rates with a voltage window of 0.01-3.0 V and using an electrochemical workstation (CHI 860 D, Beijing), respectively. Electrochemical impedance spectroscopy (EIS) measurements were performed at frequencies from 10^{-2} to 10^5 Hz.

Results and discussion

The temperature-controlled XRD patterns of the samples obtained at various reaction stages, with MoO_3 nanobelts as the precursors, are shown in Fig. 1. For the samples at annealing temperature 200, 400 ℃, only the orthorhombic MoO_3 phase (JCPDS card No. 89-7112) was found. When the reaction temperature was increased to 500 ℃, the monoclinic $Fe_2(MoO_4)_3$ phase (JCPDS card No. 72-0935) was formed and increased continuously in crystallinity at 600 ℃. Surprisingly, we noticed that the MoO_3 (060) diffraction peak was shift slightly towards higher angles (the inset of Fig. 1) with the increase of annealing temperature (before 400 ℃) in the sample. Subsequently, the (060) diffraction peak began to shift slightly towards lower angles. Since Mo atom will migrate from MoO_3 to unknown Fe source to form $Fe_2(MoO_4)_3$ phase, the Fe-doped MoO_3 will lead to the increase of d (060) [22]. Therefore, we reasonably assume that the Mo atoms first began to migrate into the Fe sources and the $Fe_2(MoO_4)_3$ began to nucleate before 400 ℃ and crystallize after 400 ℃. After that, the Fe atoms were diffused into MoO_3 crystal lattice to balance the change of interplanar spacing of (060).

To clarify the chemical reactions of the FM-500 nanowires that occur at the different reaction stages, TG-DSC analysis of the sample before calcination was carried out in air to find a suitable temperature program for obtaining FM nanowires. TG-DSC recorded in air with a heating rate of 10 ℃ min^{-1} is illustrated in Fig. S1. The details of the TG-DSC curve in the first temperature region are attributed to the loss of physisorbed water at about 136 °C. The second main weight loss corresponds to the decomposition of $Fe(OH)_3$ [23,24]. The specific process of the hydrolysis of $FeCl_3$•$6H_2O$ in aqueous solution into $Fe(OH)_3$ will be discussed in the latter section. The results show that $Fe(OH)_3$ began to decompose into Fe_2O_3 at about 363 °C. At about 500 °C in the TG-DSC curve, there is a endothermic peak, which corresponds to the formation of new phase $Fe_2(MoO_4)_3$. The result is consistent with the XRD results. After 500 °C, there is no obvious mass loss. This indicates that the sample reaches constant weight.

Fig. 2 shows the FESEM images of the samples at various reaction stages. The microstructure of the pre-synthesized MoO_3 nanobelts precursors were almost identical compared with previously reported MoO_3 nanobelts (Fig. 2a-b). When the reaction proceeded to 500 °C, many $Fe_2(MoO_4)_3$ particles were unevenly precipitated on the surfaces of the 1D MoO_3 nanowires (Fig. 2c-d). As the reaction temperature was increased to 600 °C, the sample FM-600 images are almost similar to that of sample FM-500, except for slight changes observed from Fig. 2e-f.

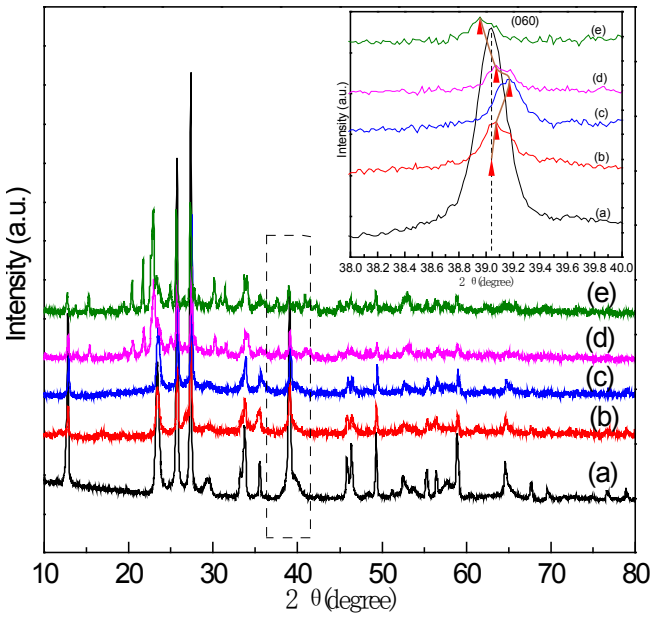

Fig. 1 XRD patterns of samples at various reaction stages, with MoO_3 nanobelts as precursors: (a)MoO_3; (b)MoO_3-200;(c)MoO_3-400; (d) FM-

500 and (e)FM-600. Inset shows shifting of the (060) diffraction peaks of MoO_3 with increasing temperature. The dashed line and arrows indicate the position of (060) diffraction peaks of MoO_3.

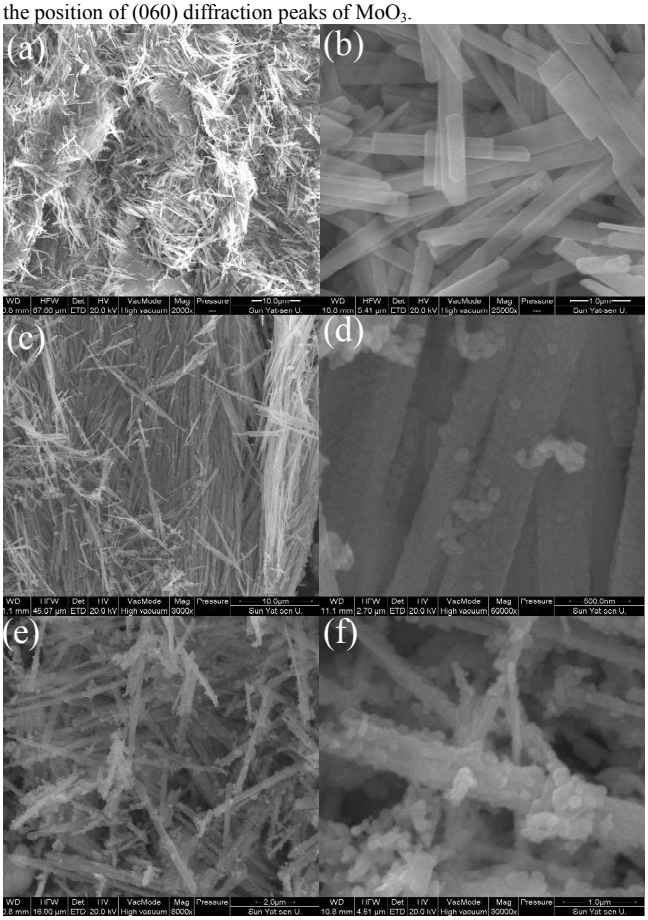

Fig. 2 FESEM images of backbone MoO_3 nanobelts (a and b), FM-500 nanowires (c and d), and FM-600 (e and f).

To explore how the $Fe_2(MoO_4)_3$ phase couples with the MoO_3 nanobelts, TEM observations of the FM-500 and FM-600 samples were conducted, respectively, as presented in Fig. 3 and Fig. S2. Fig. 3a-b show a segment of FM-500 sample. To investigate the junction between MoO_3 and $Fe_2(MoO_4)_3$, HRTEM observation was performed on the FM-500 nanowires (Fig. 3c). It is apparent that $Fe_2(MoO_4)_3$ is continuously grown with MoO_3 and it forms a distinguished interface boundary (Fig. 3a-b). The HRTEM image on the interface between the nanowires and the nanoparticles is shown as Fig. 3c. The visible lattice fringes with d spacings of 0.381and 0.388 nm, correspond to the (101) planes of MoO_3 and the (202) planes of $Fe_2(MoO_4)_3$, respectively, indicating the nanowires elongate along the [010] direction of MoO_3 and the lateral facet belongs to the {101} facets of MoO_3 nanobelts. The most clear lattice fringes for the $Fe_2(MoO_4)_3$ are from the (202) planes, which parallel to the (101) plane of MoO_3. Based on the results and the crystal knowledge of $Fe_2(MoO_4)_3$, the planes parallel to the {101} planes of MoO_3 can be formed as the requirements of crystal lattice match. The lattice mismatches between $(101)_{MoO3}$ and $(202)_{Fe2(MoO4)3}$ are ca. 1.84% [(0.388 − 0.381)/0. 381 ≈ 1.84%] (Figure, which is small enough to be tolerated for the epitaxial growth of $Fe_2(MoO_4)_3$. Significantly, the connection between $(101)_{MoO3}$ and $(202)_{Fe2(MoO4)3}$ leads to a less-defective and abrupt interface, as revealed in Fig. 3c, which is beneficial for the transfer of the charge carriers. The SAED pattern for FM-500 is consistent with the single-crystalline structures of both the MoO_3 (yellow dots) and $Fe_2(MoO_4)_3$ phases (red dots) (Fig. 3d). Fig. S3a is a scanning TEM (STEM) image of FM-500 nanowires and Fig. S3b-d show corresponding EDX elemental mapping of Fe, Mo and O, respectively. It is noticeable that O and Fe elements distribute in both the core area and the shell area. Specially, the Fe element maps from EDX further confirm the Fe elements existence within nanowires. Further, the orientation relationship between MoO_3 nanowires and $Fe_2(MoO_4)_3$ nanoparticles, as shown in Fig. 4. It should be noted that the lateral facet belongs to the {100} faces of conventional of the MoO_3 according to the literature presented method [11, 25-29]. Surprisingly, it is found that the lateral facet occurs change from {100} to {101} as $Fe_2(MoO_4)_3$ nanoparticles were formed. It is found that the morphology of MoO_3 changes from nanobelts to nanowires due to the heteroatoms diffusion and facet-selective growth of $Fe_2(MoO_4)_3$ on MoO_3 nanobelts.

Interestingly, for the sample FM-600, the increase of the diffusion rate with the assistant of increased temperature also leads to the appearance of some hollow hierarchical heterostructures, as shown in Fig.S2. For this case, by choosing the proper diffusion pairs, such as Fe and Mo, the discrepancy in diffusion rates of the two components could be utilized to generate interior voids based on mechanisms similar to the nanoscale Kirkendall effect [30]

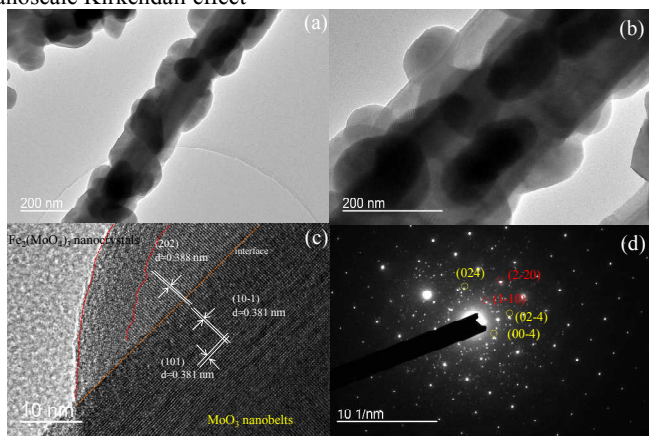

Fig. 3 Typical TEM images of an individual FM-500 nanowire (a) and (b). (c) HRTEM image of an individual FM-500 nanowire and its corresponding SAED patterns (d).

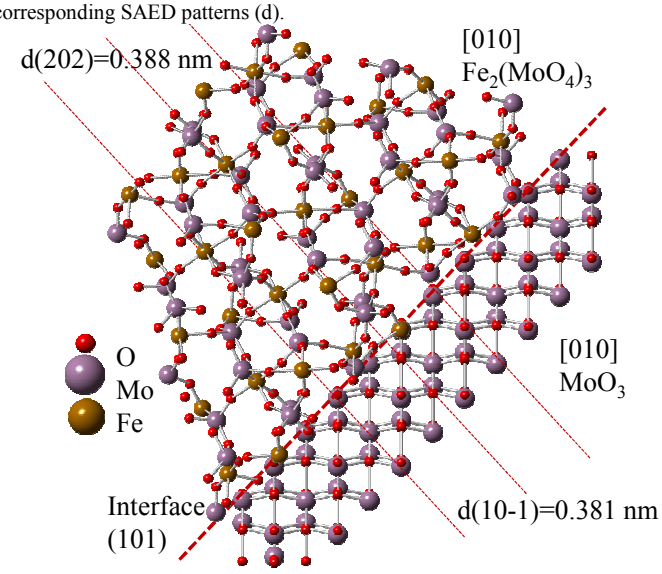

Fig.4 The orientation relationship between MoO_3 nanowires with lateral (101)facet and $Fe_2(MoO_4)_3$ nanoparticles.

Based on the XRD, FESEM and TEM analyses stated above, the formation process of the hierarchically assembled FM-500 nanowires is concluded, as illustrated in Scheme 2. First, the

MoO_3 nanobelts were coated by $FeCl_3$•$6H_2O$ colloid nanoparticles via the soaking process, which were then further converted to amorphous $Fe(OH)_3$ during the hydrolysis process of $FeCl_3$•$6H_2O$ (eq(1)), forming the $Fe(OH)_3$@MoO_3 hierarchical nanostructure (step 1).

$$FeCl_3.6H_2O=Fe(OH)_3+3HCl+3H_2O \quad (1)$$

As the reaction temperature is further increased (low than 500 ℃), the $Fe(OH)_3$ nanoparticles on the surface of MoO_3 nanobelts will aggregate and transform into Fe_2O_3 particles (eq(2)), forming the Fe_2O_3@MoO_3 hierarchical nanostructure (step 2).

$$2Fe(OH)_3=Fe_2O_3+3H_2O \quad (2)$$

As the product is thermally treated at 500 ℃, MoO_3 will fuse together with the Fe_2O_3 particles, and the reaction (eq (3)) occurs between them, accompanied with the initial nucleation of $Fe_2(MoO_4)_3$ (step 3).

$$Fe_2O_3+3MoO_3=Fe_2(MoO_4)_3 \quad (3)$$

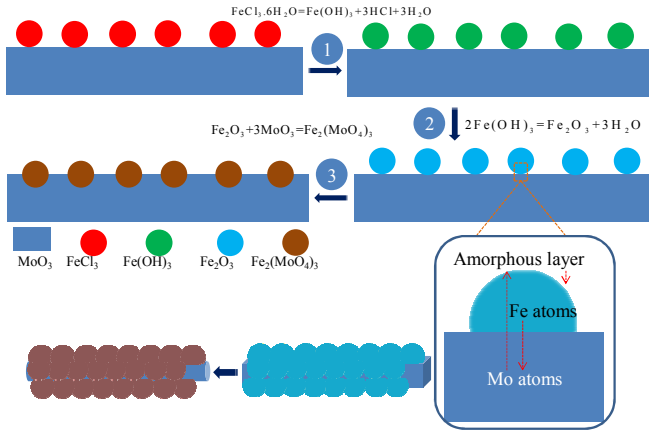

Scheme 2 Schematic illustration of the reverse heteroatoms diffusion formation mechanism for FM-500 hierarchical nanowires.

With continuous reverse heteroatoms diffusion, it is reasonable to assume that MoO_3 nanobelts may form a hollow structure, which may be due to the diffusion of Mo atoms into the Fe_2O_3 shell layers to eliminate the MoO_3 nanobelts. Our assumption is further confirmed by TEM measurements of FM-600 (Fig. S2). As expected, the hollow structure of the FM-600 is observed, as evidenced by the red arrows in Fig. S2a. The morphology evolution process of MoO_3 nanobelts is illustrated in Scheme. S1.

Chen et al reported the production of such hybrid structures and porous homogenous material $Fe_2(MoO_4)_3$ nanorods, in pursuit of enhanced ethanol sensing properties. However, it is not clear whether this unique structure is suitable for LIBs application [31, 32]. To explore the potential application of the FM-500 nanowires electrodes in LIBs, we investigated their electrochemical performance. Fig. 5 shows the galvanostatic discharge-charge voltage profiles of the three samples cycled at different rates in the voltage range of 0.01-3.0 V vs Li/Li^+. Both the two FM nanowires samples show a high initial specific capacity of 1574 and 1413 mAh g^{-1} at the current density of 50 mA g^{-1} for FM-500 and FM-600 nanowires, respectively. The results indicate the superiority of FM hierarchical nanostructures as potential high-performance anode materials for Li ion batteries. Among the three samples, the FM-500 nanowires electrode shows the best rate performance. Even at a high rate of 500 mA g^{-1}, it can still deliver a capacity of ca. 1270 mAh g^{-1}, while the MoO_3 and the FM-600 only deliver a capacity of ca. 910 and ca. 1010 mAh g^{-1}, respectively.. For clarify, the 1st discharge curves of the three samples and their corresponding dQ/dV profiles are shown in Fig. S4. Clearly, based on the voltage plateaus at ca 0.5 V for the three samples, it is found that the voltage plateaus of MF-500 and MF-600 are higher than that of the MoO_3 nanobelts, which is due to Fe^{2+}/Fe^{3+} redox levels relative to the Li/Li^+ redox level [8]. The significance of elevated voltage plateau is that it can reduce the discharge electrode polarization. Based on the above consideration, for individual MoO_3 and $Fe_2(MoO_4)_3$, the synergistic effect is very obvious. For example, for MoO_3, $Fe_2(MoO_4)_3$ can help to decrease the polarization phenomenon during the charge-discharge process due to the increase of the voltage plateau. Moreover, it can roughen the surface of the MoO_3 nanobelts and provide the electrochemical reaction sites. While for $Fe_2(MoO_4)_3$, 1D MoO_3 nanowires are a fast electron transport carrier. Additionally, the formed amorphous layer during the process of the heteroatoms reverse diffusion also helps to increase extra lithium-storage capacity and increase the lithium-ion diffusion capacity. It can be proposed that the amorphous layer surface may be rich in Mo, which may be in octahedral coordination surrounded by six oxygen atoms [33,34].

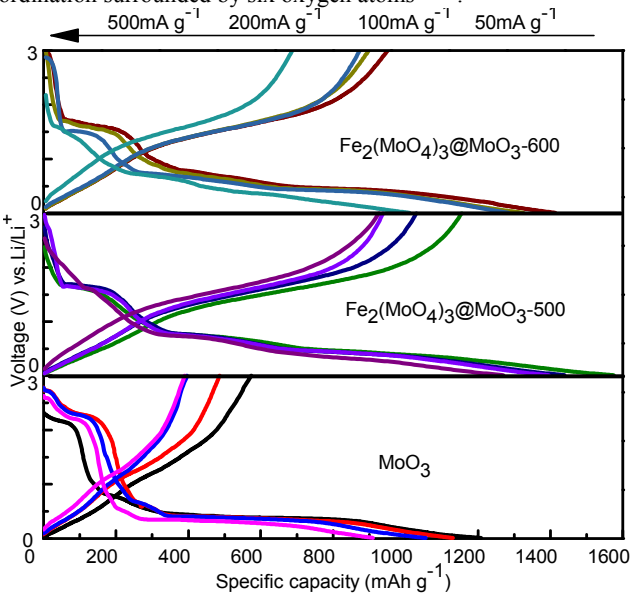

Fig. 5 The galvanostatic discharge-charge voltage profiles of the MoO_3 nanobelts, (b) FM-500 nanowires and FM-600 cycled at different rates.

Compared to MoO_3 nanobelts, the FM hierarchical nanostructure displays superior cycling performance. For example, for FM-500, it can deliver stable discharge and charge capacities of ca 585 and 580 mAh g^{-1}, respectively, after 100 cycles at the current density of 100mAh g^{-1}, as shown in Fig. 6a, whereas for the FM-600, under the identical conditions, it just delivers discharge and charge capacities of 519 and 517 mAh g^{-1}, respectively (Fig. 6a). Although the capacities decrease with increasing current density, the FM-500 nanowires still show a high capacity with excellent capacity retention even at the 200 mA g^{-1} (Fig. S5). Moreover, it is worthy of noticing that the capacity of FM first decreased and then increased with the increasing number of cycles, as shown in Fig. 6a and Fig. S5. Anomalous behaviors have been reported in previous reports [35]. Two factors may be attributed to this phenomenon: (1) the $Fe_2(MoO_4)_3$ nanoparticles have transformed into metastable lithiated orthorhombic $Li_2Fe_2(MoO_4)_3$ as the lithium ions insert in the first discharge process, while the deconstruction of the crystal $Fe_2(MoO_4)_3$ electrodes will synergistically affect the lithium storage of MoO_3 nanowires and cause capacity fading at the early stage; (2) just as mentioned above, the remaining unused active materials would be further pulverized into finer Mo nanoclusters,

which continually increases active sites as the lithium ions insert, resulting in an increased capacity with the increasing number of cycles. It can be predicted that if more cycles are applied in the cycling performance for FM, the capacity will reach a maximum and then drop, due to the full usage of active materials and the decreasing conductivity upon later cycling. The unique structure effectively enhanced lithium-ion storage capacity and improved storage kinetics, particularly at higher current density.

The rate performance of MoO_3 nanobelts and FM is also tested to study the fast discharge behaviour. As shown in Fig. 6b, the discharge rates are increased successively from 50 to 500 mA g^{-1} for each 5 cycles. For the FM, as shown in Fig. 6b, the average discharge capacities for each 5 cycles at 50, 100 and 200 mA g^{-1} are ca 1045, 708 and 558 mAh g^{-1}, respectively. At a high rate of 500 mA g^{-1}, it can still deliver a discharge capacity of ca 423 mAh g^{-1}. More surprisingly, the intercalation capability of FM-500 nanowires is over 3-fold than individual MoO_3 nanobelts in practical scenario. Moreover, the FM-500 exhibits a superior rate performance in comparison with FM-600.

Monoclinic $Fe_2(MoO_4)_3$ can theoretically accommodate up to 8 Li atoms via intercalation reaction leading to a capacity contribution of 364 mAh g^{-1} [36-38], which is lower than theoretical capacity of MoO_3. According to the traditional calculation method, the theoretical reversible capacity of FM composites should be 364-1111 mAh g^{-1}. However, the experimental reversible capacity of FM-500 nanowires is about 3 times higher than the MoO_3 nanobelts, as shown in Fig. 6a and Fig. S5. From the comparison of FM-500 nanowires, FM-600 and MoO_3 nanobelts microstructure, it is found that the FM-500 exhibited a higher specific surface area and abundant mesoporous features as a result of surface coarse treatment by the facet-selective nucleation and growth of $Fe_2(MoO_4)_3$ nanoparticles based on the Nitrogen adsorption and desorption isotherms and pore-size distribution curves (Fig. S7 and Tab. S1). No doubt, the features increase the electrochemical active sites of MoO_3. As shown in Fig. S6, a ca 10 nm thick amorphous surface layer was extended around the interface and $Fe_2(MoO_4)_3$, which can effectively hinder the side reaction between the active material and organic electrolyte cause capacity fading and safety issues.

To help understand the different lithium-storage behaviors, the lithium-ion diffusion and electron transport of the FM-500 and FM-600 are depicted in Fig. 6c-d. It is well known that 1D nanowires have attracted considerable interest and have been used in LIBs due to their unusual mechanical and electrical performance [39-47]. Obviously, compared to the rapid electron transport channel in FM-500 nanowires (Fig. 6c), FM-600 exhibits the random network at the grain boundaries, thus leading to uncontinuous electron transport (Fig. 6d). This difference between the nanowires and nanoparticles on the electrochemical properties will be disclosed in the following discussion.

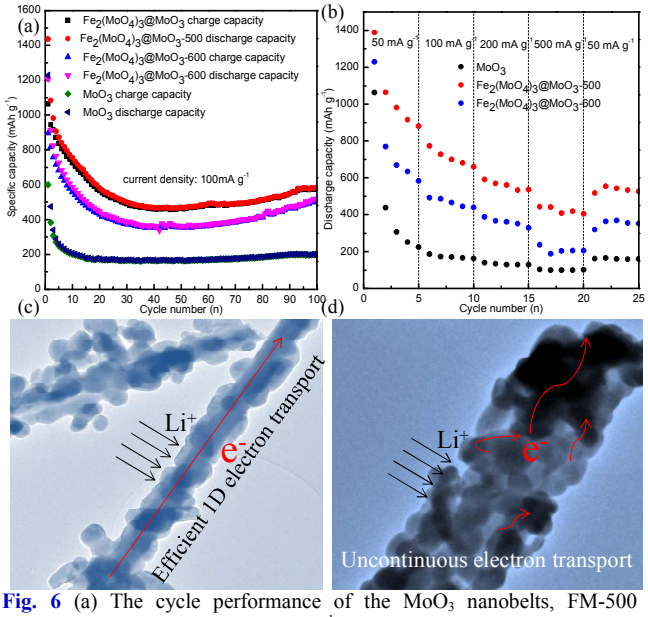

Fig. 6 (a) The cycle performance of the MoO_3 nanobelts, FM-500 nanowires and FM-600 at 100 mA g^{-1} (b) rate performance of the MoO_3 nanobelts, FM-500 nanowires and FM-600. The schematic of the charge storage advantage of the hybrid FM-500 nanowires (c) and FM-600 (d) contribute to the charge storage.

The electrochemical activity of the prepared FM electrodes was evaluated in an electrochemical measurement system and compared with that of MoO_3 nanobelts. Cyclic voltammetry (CV) results which recorded at a scan rate of 0.2 mV s^{-1} within the potential window of 0.01-3.0 V vs. Li/Li^+ is shown in Fig. 7. Obviously, FM-500 has a larger curve area and higher redox peak current than other samples, suggesting that FM-500 has the highest capacity and the fastest kinetics for Li ion insertion-extraction. The higher electrochemical activity of FM-500 nanowires may be attributed to the $Fe_2(MoO_4)_3$ modification of MoO_3 nanowires surface and the stable interface structure.

FM-500 is used as an example to explain the electrochemical process. All of these peaks originate from the phase transitions between $Li_xFe_2(MoO_4)_3$ components with different x values ($0<x<2$). Compared with CV curves of individual MoO_3 nanobelts, there are one extra oxidation peak and two reduction peaks. The extra oxidation peaks around 1.6 V correspond to the removal of the first Li in $Li_xFe_2(MoO_4)_3$, since there is an ordered $Li_xFe_2(MoO_4)_3$ phase. The extra two reduction peaks located at ca 0.6, 1.6 V. The peak ca 0.6 V may result from the reduction of $Li_xFe_2(MoO_4)_3$, associated with the Fe^{2+}/Fe^{3+} redox couple [36], which shifts to ca 0.7 V from the second cycle. The peak ca 1.6 V is ascribed to the formation of a solid electrolyte interface (SEI) layer on the electrode surface, which disappears from the second cycle. In the anodic polarization process, a broad peak centered at 1.6 V is obtained in the first and successive cycles, which is ascribed to the oxidation of Fe^{2+} [36]. For FM-500 and F-600 electrodes, besides the first cycle, the following cycles display overlapped curves, indicating the high reversibility and stability of electrodes reaction, as shown in Fig. 7b-c.

To evaluate the electrode kinetic behaviour of the MoO_3 nanobelts, FM-500 nanowires and FM-600, electrochemical impedance spectroscopy (EIS) measurements were carried out. The Nyquist plots of the three electrodes are shown in Fig. 7d. In Tab. S2, the FM-500 electrode shows a much lower charge-transfer resistance than that of the pristine MoO_3 nanobelts and FM-600 based on the equivalent circuit presented in the inset of Fig. 7d. Obviously, the R_{ct} is much smaller for the FM-500 nanowires electrode (ca 68.8 Ω) than the MoO_3 nanobelts

electrode (ca 245.5 Ω) and FM-600 electrode (ca 128.7 Ω), which are attributed to the backbone MoO_3 nanowires in FM-500 nanowires with good conductivity and efficient electron transport behavior [10]. Fig. S8 shows the charge-discharge voltage profiles for the first three charge-discharge cycles of the FM-500 nanobelts electrode at a current density of 100 mA g^{-1}. There are three voltage plateaus observed in the discharge process, which are in accordance with the redox peaks in CV curves (Fig. 7b). Additionally, as shown in Fig. 7d, FM-500 nanowires have a obvious larger slope than the MoO_3 nanobelts and FM-600, which means that the FM-500 nanowires have faster lithium-ion diffusion rates, indicating that the $Fe_2(MoO_4)_3$ nanoparticles and amorphous layer are beneficial to improve the reaction kinetics [20,48]. Furthermore, the exchange current density ($i^0 = RT/nFR_{ct}$) of the FM-500 nanowires cell was higher than those of the pristine MoO_3 nanobelts and FM-600, indicating an increase in the electrochemical active sites surface area of FM-500 nanowires due to the mesoporous features of the FM-500 nanowires. On the basis of the above analyses, the outstanding electrochemical performances of FM-500 nanowires at both low and large current densities should be ascribed to the following points: (1) the continuous interfaces formed during $Fe_2(MoO_4)_3$ growth can increase the surface area and mesoporous volume that is favorable to the electrolyte diffusion; (2) the 1D structure can not only provide more sites for the adsorption of lithium ions, but also facilitate their fast intercalation and deintercalation of active species; (3) the amorphous layer directly formed on the surface of the $Fe_2(MoO_4)_3$ nanoparticles is favorable for lithium-ion diffusion and extra storage; (4) superior to MoO_3 nanobelts, the strongly coupled $Fe_2(MoO_4)_3$@MoO_3 may synergistically enhance the electrochemical properties, such as electrical or ionic conductivity, reversible capacity, and mechanical stability. Thus, the novel FM-500 nanowires show great promise as anodes for LIBs.

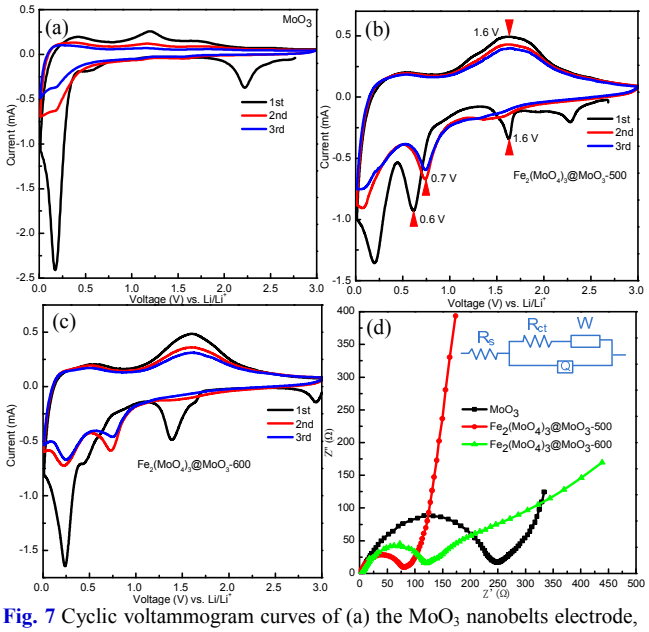

Fig. 7 Cyclic voltammogram curves of (a) the MoO_3 nanobelts electrode, (b) FM-500 nanowire electrode, (c) FM-600 electrode scanned at 0.2 mV s^{-1}.(d) Nyquist plots of the three electrodes. The inset shows the equivalent circuit.

Conclusions

In summary, for the first time FM-500 nanowires, as novel anode materials for LIBs, has been demonstrated in this study. The $Fe_2(MoO_4)_3$ nanoparticles were tightly anchored onto the surface of MoO_3 nanobelts via a heteroatom diffusion method. Importantly, a conceptually straightforward approach is developed to further enhance lithium storage capacity by introducing ternary oxide and binary oxide via a heteroatom diffusion. It may also be extended to other anode and cathode materials, such as Fe_2TiO_4@Fe_3O_4, Mn_2TiO_4@TiO_2, $NiTiO_3$@TiO_2 et al. These important findings could open up new opportunities for the design of novel electrodes in constructing high-performance energy storage devices.

Acknowledgments

This research was supported by the National Nature Science Foundations of China (No. 51462007, 41272064, 51272294), Guangxi Natural Science Foundation (No.2014GXNSFAA118349) and the National Basic Research Program of China (Grant 2012CB933704).

Notes and references

[a]*College of Materials Science and Engineering, Guilin University of Technology, Guilin 541004, PR China*
[b]*Key Laboratory of New Processing Technology for Nonferrous Metals and Materials, Ministry of Education,Guilin University of Technology, Guilin 541004, PR China*
Corresponding author. E-mail address: hbwanghai@gmail.com (H. Wang) Tel.: +86 773 5896672; fax: +86 773 5896671.

† Electronic Supplementary Information (ESI) available. See DOI: 10.1039/b000000x/

1 M.F. Hassan, Z.P. Guo, Z. Chen and H.K. Liu, J. Power Sources, 2010, **195**, 2372-2376.
2 P. Meduri, E. Clark, J.H. Kim, E. Dayalan, G.U. Sumanasekera and M.K. Sunkara, Nano Lett., 2012, **12** , 1784-1788.
3 Y.F. Dong, S. Li, H.M. Xu, M.Y. Yan, X.M. Xu, X.C. Tian, Q. Liu and L.Q. Mai, Phys. Chem. Chem. Phys., 2013, **15**, 17165-17170.
4 L.Q. Mai, B. Hu, W. Chen, Y.Y. Qi, C.S. Lao, R.S. Yang, Y. Dai and Z.L. Wang, Adv. Mater., 2007, **19**, 3712-3716.
5 X.Y. Xue, Z.H. Chen, L.L. Xing, S. Yuan and Y.J. Chen, Chem. Commun., 2011, **47**, 5205-5207.
6 C.V.S. Reddy, E.H. Walker, C. Wen and S.I. Mho, J. Power Sources, 2008, **183**, 330-333.
7 C.V.S. Reddy, Y.Y. Qi, W. Jin, Q.Y. Zhu, Z.R. Deng, W. Chen and S.I. Mho, J. Solid State Electr., 2007, **11**, 1239-1243.
8 A. Manthiram and J.B. Goodenough. J. Power Sources, 1989, **26**, 403-408.
9 Q. Sun, Q.Q. Ren and Z.W. Fu, Electrochem. Commun.,2012, **23**, 145-148.
10 A.M. Hashem, H. Groult, A. Mauger, K. Zaghib and C.M. Julien, J. Power Sources, 2012, **219**, 126-132.
11 L.L. Cai, P.M. Rao and X.L. Zheng, Nano Lett., 2011, **11**, 872-877.
12 J.S. Chen, C.M. Li, W.W. Zhou, Q.Y. Yan, L.A. Archer and X.W. Lou, Nanoscale, 2009, **1**, 280-285.
13 X.Y. Xue, B. He, S. Yuan, L.L. Xing, Z.H. Chen and C.H. Ma, Nanotechnology, 2011, **22**, 395702-395705.
14 L.L. Xing, S.A. Yuan, Z.H. Chen, Y.J. Chen and X.Y. Xue, Nanotechnology, 2011, **22**, 225502-225507.
15 L.L. Xing, S. Yuan, B. He, Y.Y. Zhao, X.L. Wu and X.Y. Xue, Chem-Asian J., 2013, **8**, 1530-1535.
16 G. Huang, F.F. Zhang, L.L. Zhang, X.C. Du, J.W. Wang and L.M. Wang, J. Mater. Chem. A, 2014, **2**, 8048-8053.
17 W. Zhou, C. Cheng, J.P. Liu, Y.Y. Tay, J. Jiang, X.T. Jia, J.X. Zhang, H. Gong, H.H. Hng, T. Yu and H.J. Fan, Adv. Funct. Mater., 2001, **21**,

2439-2445.
18 Y.L. Wang, J.J. Xu, H. Wu, M. Xu, Z. Peng and G.F. Zheng, J. Mater. Chem., 2012, **22**, 21923-21927.
19 X. Gu, L. Chen, Z.C. Ju, H.Y. Xu, J. Yang, Y.T. Qian, Adv. Funct. Mater., 2013, **23**, 4049-4056.
20 H. Wu, M. Xu, Y.C. Wang and G.F. Zheng, Nano Res., 2013, **6**, 167-173.
21 A. Phuruangrat, J.S. Chen, X.W. Lou, O. Yayapao, S. Thongtem and T. Thongtem, Appl. Phys. a-Mater., 2012, **107**, 249-254.
22 Q.Y. Ouyang, L. Li, Q.S. Wang, Y. Zhang, T.S. Wang, F.N. Meng, Y.J. Chen and P. Gao, Sensor Actuat B-Chem., 2012, **169**, 17-25.
23 Q. Wang, B.Y. Geng, S.Z. Wang, Y.X. Ye and B. Tao, Chem. Commun., 2010, **46**, 1899-1901.
24 X. Guo, H.J. Zhu, M.S. Si, C.J. Jiang, D.S. Xue and Q. Li, CrystEngComm, 2013, **1**, 8306-8313.
25 D. Xiang, C. Han, J.L. Zhang and W. Chen, Sci. Rep., 2014, **4**, 4891-4896.
26 J. Li and X.H. Liu, Mater. Lett., 2013, **112**, 39-42.
27 V.M. Mohan, W. Chen and K. Murakami, Mater. Res. Bull., 2013, **48**, 603-608.
28 Y.X. Sun, J. Wang, B.T. Zhao, R. Cai, R. Ran and Z.P. Shao, J. Mater. Chem. A, 2013, **1**, 4736-4746.
29 C.V.S. Reddy, Z.R. Deng, Q.Y. Zhu, Y. Dai, J. Zhou, W. Chen and S.I. Mho, Appl. Phys. a-Mater., 2007, **89**, 995-999.
30 Y.D. Yin, R.M. Rioux, C.K. Erdonmez, S. Hughes, G.A. Somorjai and A.P. Alivisatos, Science, 2004, **304**, 711-714.
31 Y.J. Chen, X.M. Gao, X.P. Di, Q.Y. Ouyang, P. Gao, L.H. Qi, C.Y. Li and C.L. Zhu, ACS Appl. Mater. Interfaces, 2013, **5**, 3267-3274.
32 Y. Chen, F. Meng, C. Ma, Z. Yang, C. Zhu, Q. Ouyang, P. Gao, J. Li and C. Sun, J. Mater. Chem., 2012, **22**, 12900-12906.
33 G. Sinquin, C. Petit, J.P. Hindermann and A. Kiennemann, Catal. Today, 2001, **70**, 183-196.
34 A.P.V. Soares, M.F. Portela, A. Kiennemann, L. Hilaire and J.M.M. Millet, Appl. Catal. a-Gen., 2001, **206**, 221-229.
35 Q.W. Tang, Z.Q. Shan, L. Wang and X. Qin, Electrochim. Acta, 2012, **79**, 148-153.
36 J. Shirakawa, M. Nakayama, M. Wakihara and Y. Uchimoto, J. Phys. Chem. B, 2007, **111**, 1424-1430.
37 M. Manickam, K. Minato and M. Takataz, J Electrochem. Soc., 2003, **150**, A1085-A1089.
38 A. Manthiram and J.B. Goodenough, J. Solid State Chem., 1987, **71**, 349-360.
39 S. Saadat, J.X. Zhu, D.H. Sim, H.H. Hng, R. Yazami and Q.Y. Yan, J. Mater. Chem. A, 2013, **1**, 8672-8678.
40 C.K. Chan, H.L. Peng, G. Liu, K. McIlwrath, X.F. Zhang, R.A. Huggins and Y. Cui, Nat. Nanotechnol., 2008, **3**, 31-35.
41 A.R. Armstrong, G. Armstrong, J. Canales, R. Garcia and P.G. Bruce, Adv. Mater., 2005, **17**, 862-865.
42 Y.G. Li, B. Tan and Y.Y. Wu, Nano Lett., 2008, **8**, 265-270.
43 J.Y. Liao, D. Higgins, G. Lui, V. Chabot, X.C. Xiao and Z.W. Chen, Nano Lett., 2013, **13**, 5467-5473.
44 Y.H. Wang, Y.H. Wang, D.S. Jia, Z. Peng, Y.Y. Xia and G.F. Zheng, Nano Lett., 2014, **14**, 1080-1084.
45 D.P. Cai, D.D. Wang, B. Liu, L.L. Wang, Y. Liu, H. Li, Y.R. Wang, Q.H. Li and T.H. Wang, ACS Appl. Mater. Interfaces, 2014, **6**, 5050-5055.
46 L. Yu, L. Zhang, H.B. Wu, G.Q. Zhang and X.W. Lou, Energ. Environ. Sci., 2013, **6**, 2664-2671.
47 H.W. Shim, D.K. Lee, I.S. Cho, K.S. Hong and D.W. Kim, Nanotechnology, 2010, **21**, 255706-255714.
48 X.L. Wang, W.Q. Han, H.Y. Chen, J.M. Bai, T.A. Tyson, X.Q. Yu, X.J. Wang and X.Q. Yang, J. Am. Chem. Soc., 2011, **133**, 20692-20695.